H. P. Rani
Department of Mathematics,
National Institute of Technology,
Warangal 506004, India
e-mail: hprani@nitw.ac.in

G. Janardhan Reddy
School of Physical Sciences,
Department of Mathematics,
Central University of Karnataka,
Gulbarga 585311, India
e-mail: janardhanreddy.nitw@gmail.com

Chang Nyung Kim[1]
Department of Mechanical Engineering,
College of Advanced Technology
(Industrial Liaison Research Institute),
Kyung Hee University,
Gyeonggi-do 446-701, South Korea
e-mail: cnkim@khu.ac.kr

Y. Rameshwar
Department of Mathematics,
College of Engineering,
Osmania University,
Hyderabad 500 007, India
e-mail: yrhwrr1@yahoo.co.in

Transient Couple Stress Fluid Past a Vertical Cylinder With Bejan's Heat and Mass Flow Visualization for Steady-State

In the present study, the transient, free convective, boundary layer flow of a couple stress fluid flowing over a vertical cylinder is investigated, and the heat and mass functions for the final steady-state of the present flow are developed. The solution of the time dependent nonlinear and coupled governing equations is obtained with the aid of an unconditionally stable Crank–Nicolson type of numerical scheme. Numerical results for the time histories of the skin-friction coefficient, Nusselt number, and Sherwood number as well as the steady-state velocity, temperature, and concentration are presented graphically and discussed. Also, it is observed that time required for the flow variables to reach the steady-state increases with the increasing values of Schmidt and Prandtl numbers, while the opposite trend is observed with respect to the buoyancy ratio parameter. To analyze the flow variables in the steady-state, the heatlines and masslines are used in addition to streamlines, isotherms, and isoconcentration lines. When the heat and mass functions are properly made dimensionless, its dimensionless values are related to the local and overall Nusselt and Sherwood numbers. Boundary layer flow visualization indicates that the heatlines and masslines are dense in the vicinity of the hot wall, especially near the leading edge. [DOI: 10.1115/1.4029085]

Keywords: heat function, mass function, couple stress fluid, natural convection, vertical cylinder

1 Introduction

In nature along with the free convection currents caused by the temperature differences, the flow can also be affected by the differences in concentration of the material constitution. For example, in atmospheric flows there exist differences in the H_2O concentration and hence the flow is affected by such concentration difference. In many engineering applications, some foreign gases can be injected during the convective process. This causes a reduction in the wall shear stress, the mass transfer conductance or the rate of heat transfer. Usually, H, H_2, O, CO_2, etc., are the foreign gases which are injected in the air. Sometimes, an evaporating material is coated on the surface of the body and some of the contents of this material evaporate due to the heating of the body and mix with the fluid that passes over this body. Thus, the free convective flow with mass transfer plays a key role in day to day applications.

Considerable attention has been paid to the problem of steady natural convective flow over a vertical cylinder. Sparrow and Gregg [1] studied one such problem of steady free convective flow past a vertical cylinder where the temperature of the cylinder surface was taken to be uniform. Minkowycz and Sparrow [2] applied the local nonsimilarity solution method to solve the similar problem for uniform thermal condition. Fujii and Uehara [3] analyzed the local heat transfer results for arbitrary Prandtl number. Lee et al. [4] investigated the problem of natural convection in a laminar boundary layer flow along slender vertical cylinders for the power-law variation in wall temperature. Bottemanne [5] and Chen and Yuh [6] presented the experimental and analytical studies for the simultaneous heat and mass transfer by free convection about a vertical cylinder. Gebhart and Pera [7] analyzed the steady combined buoyancy effects on vertical natural convection flows. Transient natural convection from thin vertical cylinders was studied by Dring and Gebhart [8] by using the quasi-static technique. The same problem was considered by Evan et al. [9] both experimentally and analytically. Recently, Rani and Kim [10] investigated the Dufour and Soret effects on unsteady natural convection flow past an isothermal vertical cylinder. The present physical model has applications in the glass and polymer industries, hot filaments, are considered as vertical cylinders. These cylinders are cooled as they pass through the surrounding environment. In most of these situations, the temperature distribution in the fluid is mutually coupled to the temperature distribution in the solid body over which the fluid flows.

It can be noted that many of the above mentioned convective flows caused by to the combined buoyancy effects of thermal and species (concentration) diffusions deal with the fluids which obey the Newtonian relationship. While, in many of the real fluids the shear behavior is characterized by the non-Newtonian relationship. The diverse non-Newtonian fluid theories emerged to explain the deviation in the behavior of real fluids from that of the Newtonian fluids. Two such fluid theories, which are popular, are those proposed by Eringen [11] and Stokes [12] and these are, respectively, referred to as the micropolar and couple stress fluid theories. Five decades have passed ever since the theory of couple stress fluids was initiated by Stokes [12] in 1966. This simplest couple stress theory reveals all the important features and effects of couple stresses, thereby facilitating a comparison with the results for the classical nonpolar case. The main effect of couple stresses is to introduce a size dependent effect based on the material constant and dynamic viscosity, which is not present in the classical viscous theories. The fluids consisting of rigid, randomly oriented particles suspended in a viscous medium, such as blood, lubricants containing small amount of polymer additive, electrorheological fluids, and synthetic fluids are some of the examples

[1]Corresponding author.

Contributed by the Heat Transfer Division of ASME for publication in the Journal of Heat Transfer. Manuscript received August 24, 2013; final manuscript received October 25, 2014; published online December 17, 2014. Assoc. Editor: Danesh / D. K. Tafti.

for these fluids. Also, some more examples are the extrusion of polymer fluids, solidification of liquid crystals, cooling of metallic plate in a bath, colloidal solutions, etc. Recently, the study of couple stress fluid flows has been the subject of great interest, due to its widespread industrial and scientific applications as in the case of micropolar fluids. Important fields where the couple stress fluids have applications include squeezing and lubrication [13–16], biofluidmechanics [17,18], Magneto Hydrodynamic (MHD) flows, and synthesis and plasticity of chemical compounds. Another interesting application was studied by Umavathi and Malashetty [19] for the flow and heat transfer characteristics of Oberbeck convection of a couple stress fluid in a vertical porous stratum. In the presence of mass transfer, Habtu and Radhakrishnamacharya [20] studied the dispersion of a solute in the peristaltic motion of a couple stress fluid through a porous medium in the presence of mass transfer. They observed that the effective dispersion coefficient increases along with permeability parameter but decreases with homogeneous chemical reaction, couple stress, slip and heterogeneous reaction parameters. In the presence of chemical reaction, recently, Tasawar et al. [21] analyzed the transient three-dimensional flow of couple stress fluid over a stretched surface in the presence of chemical reaction.

From the literature, it can be seen that the problem of unsteady combined heat and mass transfer by natural convective couple stress fluid flow over a semi-infinite vertical cylinder has received very scant attention owing to its mathematical difficulty in solving the unsteady governing equations. Hence, it is proposed to study the transient couple stress fluid flow past a vertical cylinder with combined heat and mass transfer effects. The present problem formulation, the surface temperature and concentration are considered to be higher than those of ambient fluid temperature and concentration, respectively. The nondimensional unsteady nonlinear partial differential equations which govern the flow are solved numerically by using the finite difference method. The transient effects of the couple stress fluid flow are analyzed based on the average skin-friction coefficient, heat and mass transfer rates for different parameters, and the comparison of couple stress fluid flow and Newtonian fluid flow is performed. The results obtained in this study compared with the relevant results in the existing literature, showing good agreement.

In general, studies on the natural convection have been carried out with streamlines, isotherms, and isoconcentration lines. Isotherms and isoconcentration lines are generally used to illustrate the temperature and concentration distribution in a domain, respectively. However, isotherms and isoconcentration lines may not be suitable to visualize the direction and intensity of heat and mass transfer particularly in convection problems in which the path of heat and mass flux is not perpendicular to isotherms and isoconcentration lines, respectively, due to the convection effect. When dealing with the two-dimensional fluid flows, it is not the isobars but the streamlines that are the best tools for visualization and analysis, as the fluid flows are not in the direction perpendicular to the isobars. Similarly, when dealing with the two-dimensional convective heat and mass transfer, it is not the isotherms and isoconcentration lines but the heatlines and masslines that are the best tools for visualization and analysis. The main use of heatlines and masslines is to find the intensity of heat and mass transfer that may not be observed by other tools such as velocity, temperature, and concentration. The heatlines and masslines are the adequate tools for visualization and analysis of the heat and mass transfer process, giving well defined corridors where energy and concentration transfer occur from the hot wall toward the cold wall.

Heatlines and masslines are the contours of the heat and mass functions, respectively, and the proper dimensionless forms of heat and mass functions are related to the local and overall Nusselt and Sherwood numbers. The heatline concept was first introduced by Kimura and Bejan [22] and Bejan [23], and its mass counterpart, the massline concept, by Trevisan and Bejan [24]. Costa [25] investigated the heatline and massline visualization for natural convection boundary layers near a vertical wall. A detailed review on the applications of heatlines and masslines was also performed by Costa [26]. The use of heatlines in the unsteady problems was first studied by Aggarwal and Manhapra [27,28] to analyze the unsteady heat transfer process in cylindrical enclosures subjected to the natural convection. Extension of the concept of heatlines and masslines to reacting flows through the use of conserved scalars has been proposed by Mukhopadhyay et al. [29]. Recently, Basak et al. [30] studied the analysis of heatlines within triangular cavities. Till date, the heatlines and masslines concepts have not been used extensively for analyzing convective heat and mass transport processes except for very few applications. Based on this literature survey, for the first time an attempt is made to study the concept of heatlines and masslines to the present investigated problem at the final steady-state.

2 Mathematical Formulation

A transient two-dimensional laminar combined heat and mass transfer boundary layer flow of a couple stress viscous incompressible fluid past a semi-infinite, vertical, isothermal cylinder of radius r_0 is considered as shown in Fig. 1. It is assumed that the effect of viscous dissipation is negligible in the energy equation since the flow velocity magnitude is expected to be small. The concentration C_0 of the diffusing species is assumed to be very small in the binary mixture, and there is no chemical reaction between the diffusing species and the fluid. The x-axis is measured vertically upward along the axis of the cylinder. The origin of x is taken to be at the leading edge of the cylinder, where the boundary layer thickness is zero. The radial coordinate, r, is measured perpendicular to the axis of the cylinder. The surrounding stationary fluid has temperature T'_∞ and concentration C'_∞. Initially, it is assumed that the cylinder and the fluid are of the same temperature and concentration. The temperature of the cylinder is suddenly raised to $T'_w\left(> T'_\infty\right)$ and concentration near the cylinder is also raised to $C'_w\left(> C'_\infty\right)$. Then they are maintained at the same level for all time $t' > 0$.

Due to this temperature and concentration gradients in fluid region near the cylinder, density difference is created, leading to a natural convection in the presence of gravitation. Hence, there occurs a natural convection flow. The transition of velocity, temperature, and concentration occurs in a thin layer adjacent to cylinder wall, which is termed as a boundary layer. Under the above assumptions, the boundary layer equations of mass, momentum, energy, and species concentration with Boussinesq's approximation are as follows:

$$\frac{\partial(ru)}{\partial x} + \frac{\partial(rv)}{\partial r} = 0 \tag{1}$$

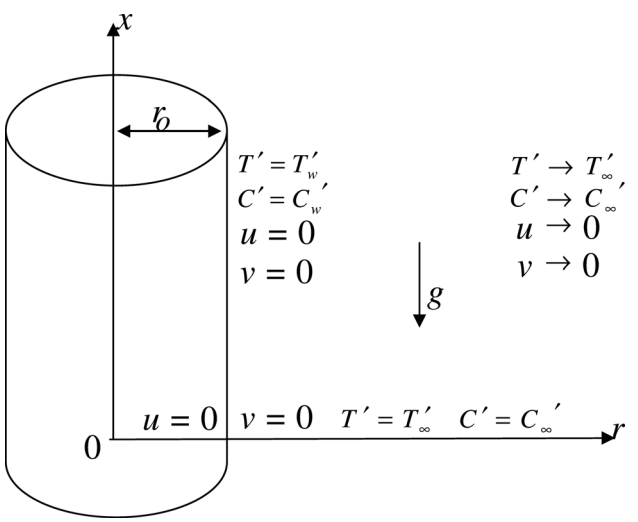

Fig. 1 Schematic of the investigated problem

$$\rho\left(\frac{\partial u}{\partial t'}+u\frac{\partial u}{\partial x}+v\frac{\partial u}{\partial r}\right)=\rho g\beta_T\left(T'-T'_\infty\right)+\rho g\beta_C\left(C'-C'_\infty\right)+\frac{\mu}{r}\frac{\partial}{\partial r}\left(r\frac{\partial u}{\partial r}\right)-\eta\nabla^4 u \tag{2}$$

$$\frac{\partial T'}{\partial t'}+u\frac{\partial T'}{\partial x}+v\frac{\partial T'}{\partial r}=\frac{\alpha}{r}\frac{\partial}{\partial r}\left(r\frac{\partial T'}{\partial r}\right) \tag{3}$$

$$\frac{\partial C'}{\partial t'}+u\frac{\partial C'}{\partial x}+v\frac{\partial C'}{\partial r}=\frac{D}{r}\frac{\partial}{\partial r}\left(r\frac{\partial C'}{\partial r}\right) \tag{4}$$

The constitutive equations concerning the force stress tensor t_{ij} and the couple stress tensor m_{ij} that arises in the theory of couple stress fluids are given by [12]

$$t_{ij}=(-p+\lambda\nabla.\mathbf{U})\delta_{ij}+2\mu d_{ij}-\frac{1}{2}\varepsilon_{ijk}\left[m_{ij}+4\eta\omega_{k,rr}+\rho c_k\right] \tag{5}$$

$$m_{ij}=\frac{1}{3}m\delta_{ij}+4\eta'\omega_{j,i}+4\eta\omega_{i,j} \tag{6}$$

In the above Eqs. (5) and (6), $\mathbf{U}$ is the velocity vector, $\omega(=(1/2)\nabla\times\mathbf{U})$ is the spin vector, $\omega_{i,j}$ is the spin tensor, d_{ij} is the rate of deformation tensor, $m(=m_{11}+m_{22}+m_{33})$ is the trace of the couple stress tensor m_{ij}, p is the fluid pressure, δ_{ij} is the Kronecker delta, ε_{ijk} is the Levi-Civita symbol, and ρc_k is the body couple vector. Comma in the suffixes denotes covariant differentiation and $\omega_{k,rr}$ stands for $\omega_{k,11}+\omega_{k,22}+\omega_{k,33}$.

The quantities λ and μ are the viscosity coefficients and η,η' are the couple stress viscosity coefficients. These material constants are constrained by the following inequalities:

$$\mu\geq 0;3\lambda+2\mu\geq 0;\eta\geq 0;|\eta'|\leq\eta \tag{7}$$

Usually, the ratio of material constants η and μ has the dimensions of length square, i.e., $l^2(=\eta/\mu)$. It can be identified to be a property that depends on the size of the fluid molecule [31].

Stokes [32] proposed mainly two types of boundary conditions, namely, the vorticity of the fluid on the boundary is equal to the rotational velocity of the boundary and the couple stresses vanish on the boundary. The present problem is solved based on the former boundary condition, i.e., $\nabla\times\mathbf{U}=0$. In view of this, the relevant initial and boundary conditions are given by

$$\begin{array}{rrrrrr} t'=0: & u=0, & v=0, & T'=T'_\infty, & C'=C'_\infty & \text{for all } x \text{ and } r \\ t'>0: & u=0, & v=0, & T'=T'_w, & C'=C'_w & \text{at } r=r_0 \\ & u=0, & v=0, & T'=T'_\infty, & C'=C'_\infty & \text{at } x=0 \\ & u\to 0, & v\to 0, & T'\to T'_\infty, & C'\to C'_\infty & \text{as } r\to\infty \end{array} \tag{8}$$

$$\frac{\partial u}{\partial r}=\frac{\partial v}{\partial x} \quad \text{at} \quad r=r_0 \quad \text{and} \quad \text{as} \quad r\to\infty$$

By introducing the following nondimensional quantities

$$X=\mathrm{Gr}_T^{-1}\frac{x}{r_0},\quad R=\frac{r}{r_0},\quad U=\mathrm{Gr}_T^{-1}\frac{ur_0}{\nu},\quad V=\frac{vr_0}{\nu},\quad t=\frac{\nu t'}{r_0^2},$$
$$T=\frac{T'-T'_\infty}{T'_w-T'_\infty},\quad C=\frac{C'-C'_\infty}{C'_w-C'_\infty},\quad \mathrm{Gr}_T=\frac{g\beta_T r_0^3\left(T'_w-T'_\infty\right)}{\nu^2},$$
$$\mathrm{Gr}_C=\frac{g\beta_C r_0^3\left(C'_w-C'_\infty\right)}{\nu^2},\quad \mathrm{Pr}=\frac{\nu}{\alpha},\quad \mathrm{Sc}=\frac{\nu}{D},\quad \mathrm{Bu}=\frac{\mathrm{Gr}_C}{\mathrm{Gr}_T} \tag{9}$$

(the symbols are explained in the Nomenclature section) in the Eqs. (1)–(4), the following equations are obtained:

$$\frac{\partial U}{\partial X}+\frac{\partial V}{\partial R}+\frac{V}{R}=0 \tag{10}$$

$$\frac{\partial U}{\partial t}+U\frac{\partial U}{\partial X}+V\frac{\partial U}{\partial R}=T+\mathrm{Bu}C+\frac{\partial U}{\partial R}\left(\frac{1}{R}-\frac{1}{R^3}\right)+\frac{\partial^2 U}{\partial R^2}\left(1+\frac{1}{R^2}\right)-\frac{2}{R}\frac{\partial^3 U}{\partial R^3}-\frac{\partial^4 U}{\partial R^4} \tag{11}$$

$$\frac{\partial T}{\partial t}+U\frac{\partial T}{\partial X}+V\frac{\partial T}{\partial R}=\frac{1}{\mathrm{Pr}}\left(\frac{\partial^2 T}{\partial R^2}+\frac{1}{R}\frac{\partial T}{\partial R}\right) \tag{12}$$

$$\frac{\partial C}{\partial t}+U\frac{\partial C}{\partial X}+V\frac{\partial C}{\partial R}=\frac{1}{\mathrm{Sc}}\left(\frac{\partial^2 C}{\partial R^2}+\frac{1}{R}\frac{\partial C}{\partial R}\right) \tag{13}$$

The corresponding initial and boundary conditions in nondimensional quantities are given by

$$\begin{array}{rrrrrr} t=0: & U=0, & V=0, & T=0, & C=0 & \text{for all } X \text{ and } R \\ t>0: & U=0, & V=0, & T=1, & C=1 & \text{at } R=1 \\ & U=0, & V=0, & T=0, & C=0 & \text{at } X=0 \\ & U\to 0, & V\to 0, & T\to 0, & C\to 0 & \text{as } R\to\infty \end{array} \tag{14}$$

$$\frac{\partial U}{\partial R}=\frac{1}{\mathrm{Gr}_T^2}\frac{\partial V}{\partial X} \quad \text{at} \quad R=1 \quad \text{and} \quad \text{as} \quad R\to\infty$$

3 Numerical Procedure

An implicit finite difference scheme of Crank–Nicolson type has been used to solve the governing nondimensional equations (10)–(13) under the initial and boundary conditions (14). The method of solving the above unsteady, nonlinear coupled equations (10)–(13) by using the Crank–Nicolson type has been discussed in Ref. [33]. The region of integration is considered as a rectangle with sides $X_{\min}=0$, $X_{\max}=1$, $R_{\min}=1$, and $R_{\max}=20$, where $R_{\max}$ corresponds to $R=\infty$ which lies very well outside the momentum, thermal, and concentration boundary layers. The maximum value of R was chosen as 20 after some preliminary investigations so that the last three lines mentioned in the boundary conditions (14) are satisfied within the tolerance limit of 10^{-5}. The mesh density has been varied so that the computed solutions represent the real flow physics. In order to obtain an economical and reliable grid system for the computations, a grid independency test has been performed and shown in Fig. 2. The steady-state velocity, temperature, and concentration values obtained with the grid system of 100×500 differ in

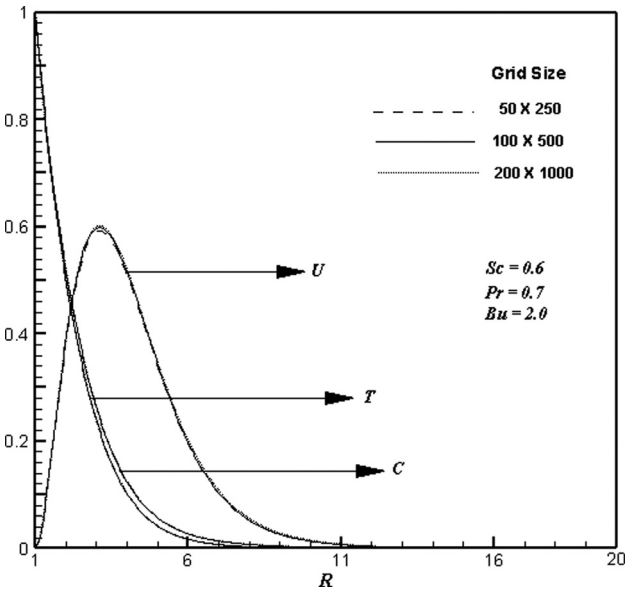

Fig. 2 Grid independent test

the second decimal place from those with the grid system of 50×250, and differ in the fifth decimal place from those with the grid system of 200×1000. Hence, in the present analysis, for more accurate results, which is close to the physically reasonable results, the fine grid size 100×500 was selected as the optimal mesh for all subsequent analyses, with mesh size in X and R directions are taken as 0.01 and 0.04, respectively. Also, the time step size dependency has been carried out, from which 0.01 yielded a reliable result. The steady-state solution is assumed to have been reached when the absolute difference between the values of velocity, temperature as well as concentration at two consecutive time steps is less than 10^{-5} at all grid points.

4 Results and Discussion

To validate the present numerical method, the temperature and concentration profiles of Newtonian fluids obtained by the current numerical procedure are compared with the existing results of Chen and Yuh [6] for $Sc = 0.2$, $Pr = 0.7$, and $Bu = 1.0$, as there are no experimental or analytical studies available to corroborate the present problem. The current results are found to be in good agreement with the previous results available in the literature as shown in Fig. 3. These results corroborate the validity and accuracy of the present numerical solution.

Numerical calculations were carried out and the results are shown graphically. The effects of nondimensional parameters like, Prandtl number (Pr), Schmidt number (Sc), and buoyancy ratio parameter (Bu) on the nature of the flow transport are analyzed. Natural convection flows driven by the combination of multiple buoyancy effects are very important in many applications. The foregoing formulations are analyzed to indicate the nature of the interaction of multiple contributions to buoyancy. Each of multiple contributions may aid or oppose and may have a magnitude different from others. Only the aiding effects, i.e., the positive values of Bu, are considered in the present study. Good examples for these types of problems include the environmental chambers with heated walls and the free convection flow associated with heat-rejection systems for long duration deep ocean power modules where the ocean environment is stratified. In view of some of these examples, the results are limited to those of Prandtl numbers of 0.7 (for air) and 7.0 (for water). In the air, the diffusing chemical species of most common interest have Schmidt numbers in the range from 0.1 to 1.0. Therefore, this range is considered with Sc (0.6 (water vapor) and 0.94 (carbon dioxide)) (see Ref. [6]). In Secs. 4.1–4.4, the simulated transient behavior of the dimensionless velocity, temperature, concentration, average skin-friction coefficient, and heat and mass transfer rates is discussed in detail in Secs. 4.1–4.4 along with streamlines, heatlines, and masslines at the final steady-state are investigated.

4.1 Flow Variables. To analyze the transient behavior of the simulated flows variables, such as velocity, temperature, and concentration, their values are depicted at different locations, which are close to the cylinder wall. The steady-state velocity, temperature, and concentration profiles are shown along the radial coordinate at $X = 1.0$. It is observed that the time required for the flow variables to reach the steady-state increases with the increasing values of Sc and Pr, while the opposite trend is observed for Bu.

Velocity. The simulated transient velocities (U) at the point (1, 3.09) for various Sc, Pr, and Bu against t are shown graphically in Fig. 4(*a*). It is observed that for all parameter values the velocity increases with time monotonically from zero and reaches temporal

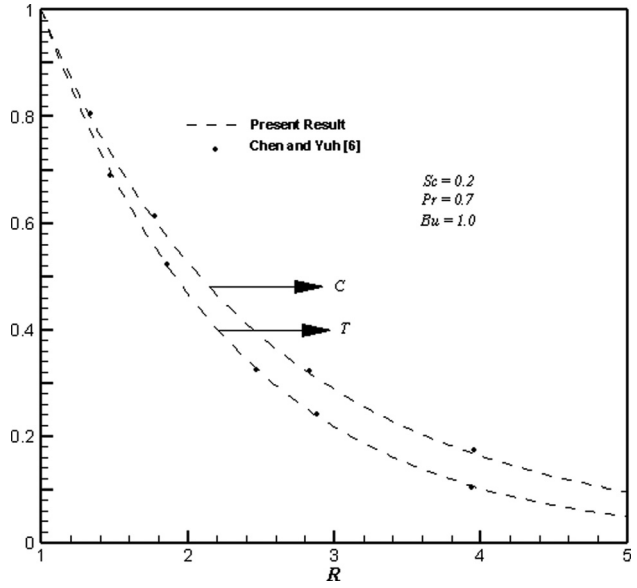

Fig. 3 Comparison of the temperature and concentration profiles

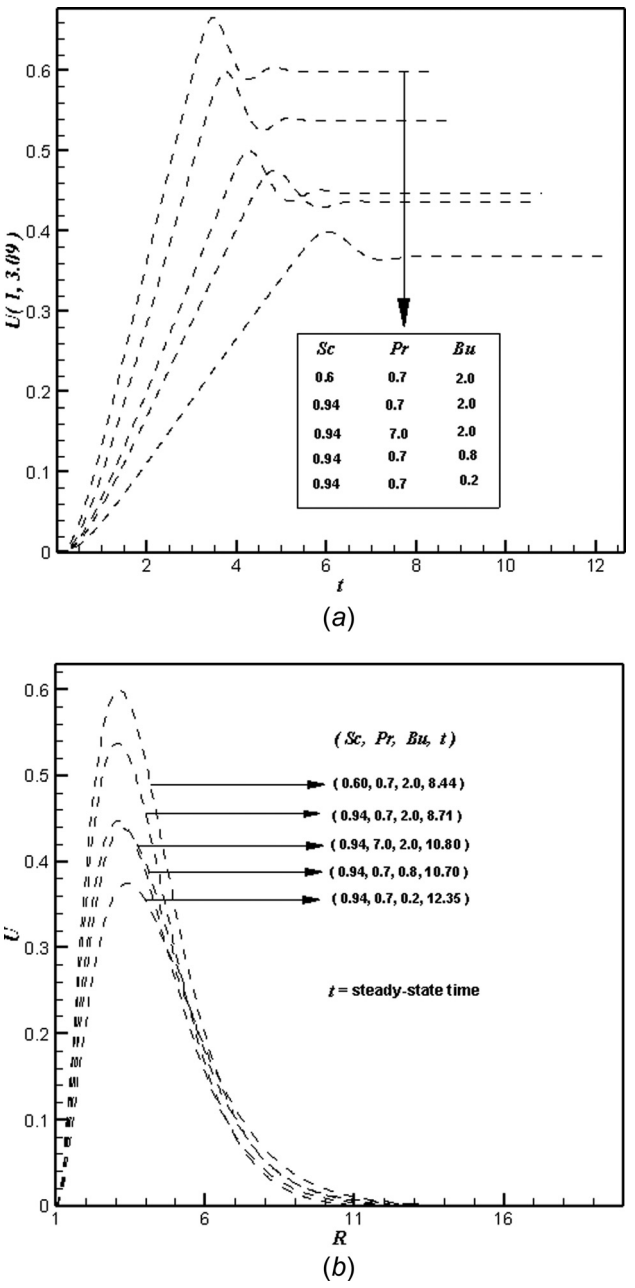

Fig. 4 The simulated (*a*) transient velocity (U) at the point (1, 3.09) and (*b*) steady-state velocity (U) profile at $X = 1.0$

maxima, then decreases and at last reaches the asymptotic steady-state. At the very early time (i.e., $t \ll 1$), the heat transfer is dominated by conduction. Shortly later, there exists a period when the heat transfer rate is influenced by the effect of convection with increasing upward velocities with time. When this transient period is almost ending and just before the steady-state is about to be reached, there exist overshoots of the velocities. Similarly, the velocities at other locations also exhibit somewhat similar transient behavior.

Figure 4(*b*) shows the simulated steady-state velocity profiles against the R at $X = 1.0$. From this figure, it is observed that the velocity profiles start with the value zero at the wall, reach their maxima and then monotonically decrease to zero along the radial coordinate. Also, in the vicinity of the wall, the magnitude of the axial velocity is rapidly increasing as R increases from $R_{\min}$ ($= 1$). The time required to reach the steady-state increases as Sc and Pr increases. Here, the velocity decreases with increasing values of Sc and Pr, because the thermal and/or concentrative convections are confined to a region near the wall with higher Pr and/or Sc (Refer to Fig. 5(*b*)). These results show that the radial position for the peak axial velocity move toward the wall as Pr and/or Sc are increased, as can be seen in Fig. 4(*b*). In a situation where Pr and Sc are given, the size of the peak velocity is larger for larger Bu (see Fig. 4(*b*)) since the term BuC in the RHS of Eq. (11) becomes larger with larger C, yielding higher axial velocity.

Temperature. The simulated transient temperatures (T) profiles for different Sc, Pr and Bu with respect to t are shown at the point (1, 1.34) in Fig. 5(*a*). Here, at the beginning that these profiles increase with time, reach temporal maxima, decrease, and after a slight increase, attain the steady-state asymptotically. The temperatures at the other locations also exhibit somewhat similar transient behavior. During the initial period, the nature of the transient temperature profiles is particularly noticeable. For small value of Pr (=0.7), the transient temperature profiles initially coincide and then deviate from each other after some time. Here, it is observed that the steady temperature value decreases with increasing values of Pr for fixed Sc and Bu. This tendency is also found in Fig. 5(*b*) showing the simulated steady-state temperature profiles along the radial direction at $X = 1.0$. Here, the temperature profiles start with the hot wall temperature ($T = 1$) and then monotonically decrease to zero along the radial coordinate. As mentioned before, as Pr increases the thickness of the thermal boundary layer is decreased with an increased temperature gradient near the wall, which moves the radial position for the peak axial velocity toward the wall. The time required for the temperature to reach the steady-state increases as Pr increases. Also, the time required to reach the temporal maximum of the temperature increases with increasing values of Pr. Larger Pr values give rise to thinner thermal boundary layer since a larger Pr value means that the thermal diffusion from the wall is not prevailing, while the velocity diffusion is noticeable even away from the wall. As the value of Bu decreases, the temperature profiles increase with the decreased axial velocity profile (Refer to Fig. 4(*b*)). It is also observed that the temperature increases as Sc increases for fixed values of Pr and Bu.

Concentration. The simulated transient concentrations (C) for different values of Sc, Pr, and Bu at the point (1, 1.34) against t are shown in Fig. 6(*a*). Here, it is observed that these profiles increase at first with time, reach temporal maxima, decrease, and after slightly increasing, attain the steady-state asymptotically. The concentrations at other locations also exhibit somewhat similar transient behavior. It is observed that the temporal maxima are attained at an early stage for small values of Sc. Here, it is seen that the steady concentration value decreases with increasing values of with fixed Pr and Bu. The simulated steady-state concentration profiles at $X = 1.0$ along the R direction at $X = 1.0$ are shown in Fig. 6(*b*). The concentration profiles start with the wall concentration ($C = 1$) and then monotonically decrease to zero along R. As Sc increases, the mass transfer rate increases and hence the concentration profiles decrease. This is due to the fact that a larger

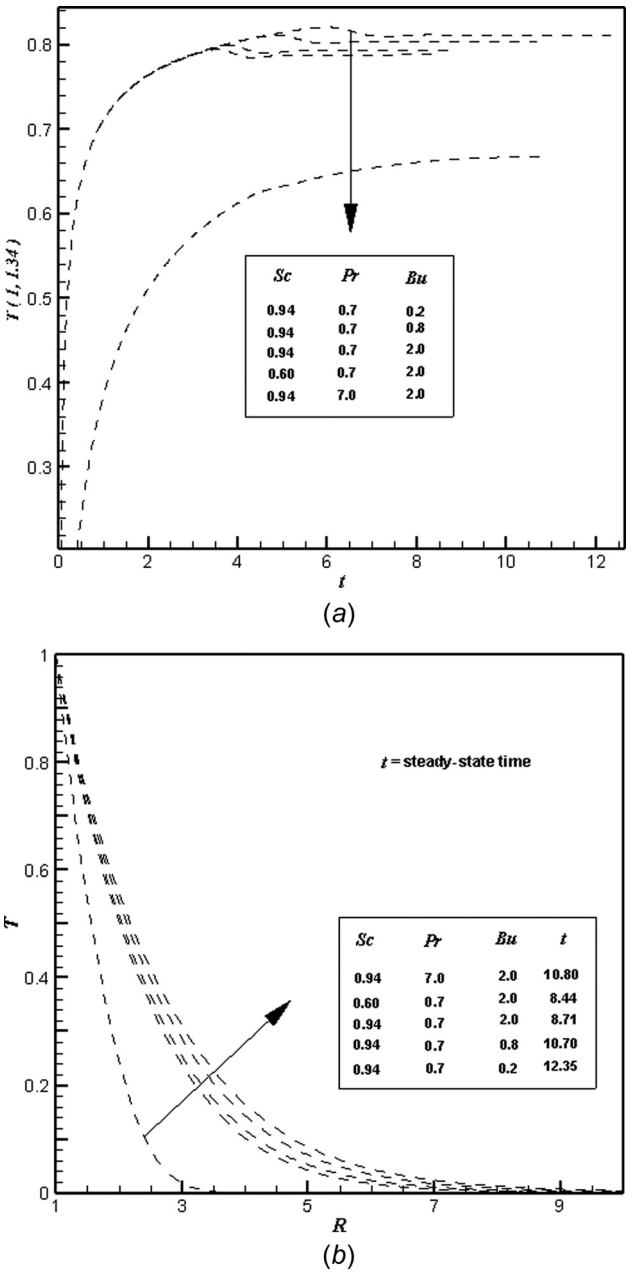

Fig. 5 The simulated (*a*) transient temperature (T) at the point (1, 1.34) and (*b*) steady-state temperature (T) profile at $X = 1.0$

Sc corresponds to a thinner concentration boundary layer relative to the momentum boundary layer. This results in a larger concentration gradient near the cylinder. It can be noticed that the concentration profiles increase as Bu decreases, since the axial velocity is decreased with a decrease in Bu (Refer to Eq. (11)). Also, it is observed that as Pr increases the concentration profiles increases.

4.2 Average Momentum, Heat and Mass Transport Coefficients. Knowing the unsteady behavior of velocity, temperature, and concentration profiles from the solution of the Eqs. (10)–(13) along with the initial and boundary conditions given in Eq. (14), it is worth studying the behavior of average skin-friction coefficient (wall shear stress), average heat transfer rate (Nusselt number), and the average mass transfer rate (Sherwood number) with respect to different parameters. For the present problem, these nondimensional average skin-friction coefficient, Nusselt number,

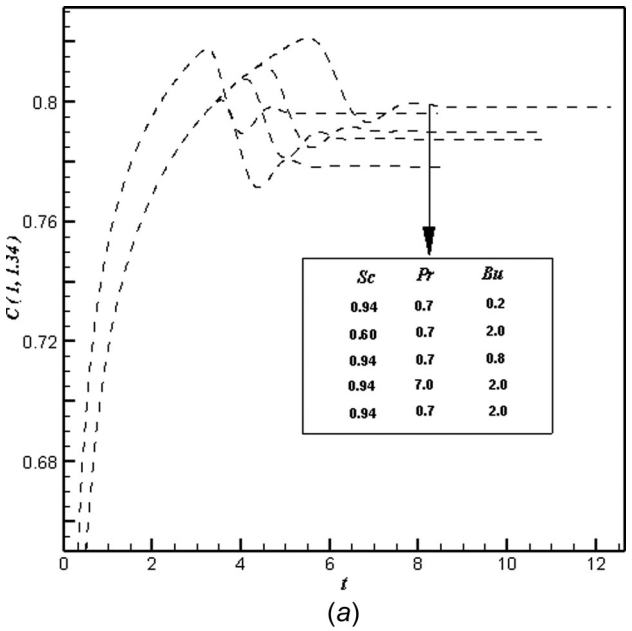

(*a*)

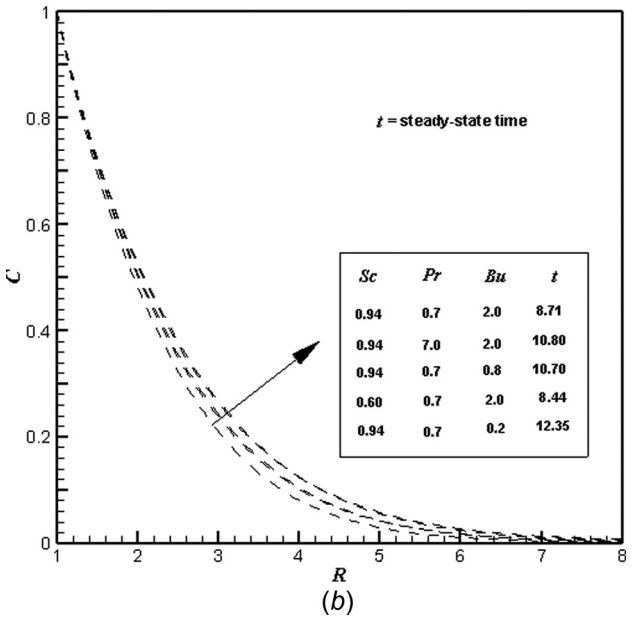

(*b*)

Fig. 6 The simulated (*a*) transient concentration (*C*) at the point (1, 1.34) and (*b*) steady-state concentration (*C*) profile at *X* = 1.0

and Sherwood number are given by $\overline{C_f} = \int_0^1 ((\partial U/\partial R))_{R=1} dX$, $\overline{\mathrm{Nu}} = -\int_0^1 ((\partial T/\partial R))_{R=1} dX$, and $\overline{\mathrm{Sh}} = -\int_0^1 ((\partial C/\partial R))_{R=1} dX$, respectively. The derivatives are evaluated by using a five-point approximation formula and then the integrals are evaluated by using the Newton-Cotes closed integration formula. The simulated average nondimensional skin-friction coefficient, heat and mass transfer rates for couple stress fluids have been plotted against the time in Figs. 7, 9, and 10 for different parameters, respectively.

The effects of Sc, Pr, and Bu on the simulated average skin-friction coefficient are shown in Fig. 7. It is observed that for all values of Sc, Pr, and Bu the average skin-friction coefficients initially increase with respect to time, attain the peak values and, after slight decrease, reach steady-state asymptotically. It is also observed that for increasing values of Sc and Pr the average skin-friction coefficient decreases. This result lies in the same line with the velocity profiles plotted in Fig. 4. Also, it is noticed that the average skin-friction is decreased with decreasing values of Bu, because the axial velocity is decreased with a decrease in Bu.

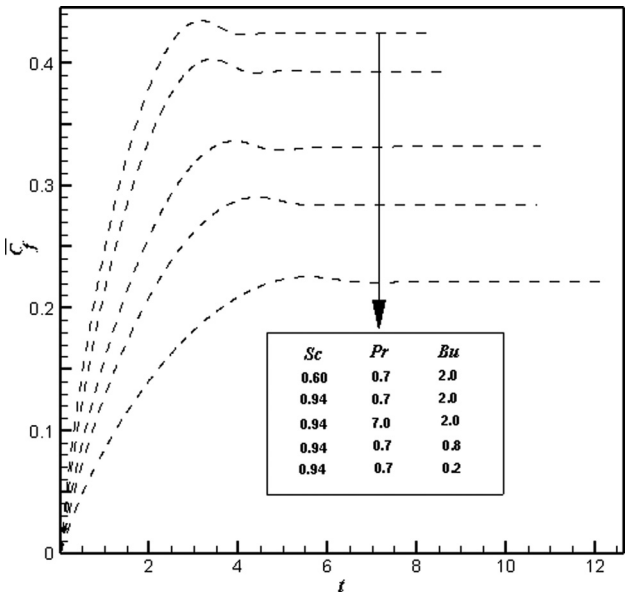

Fig. 7 The simulated average skin-friction coefficient ($\overline{C_f}$)

In order to assess the accuracy of the numerical results, the local Nusselt and Sherwood number obtained by the present simulation for Newtonian fluids are also compared with those of Chen and Yuh [6] with Pr = 0.7, Sc = 1.0, and Bu = 1.0 and these are shown in Fig. 8. Also, the authors have compared the skin-friction coefficient, Nusselt number, and Sheerwood number obtained by the present work with those of the previously published work of Ganesan and Rani [33] for Newtonian fluid in tabular form as shown in Table 1. The agreement between the previous and the present numerical results is found to be good.

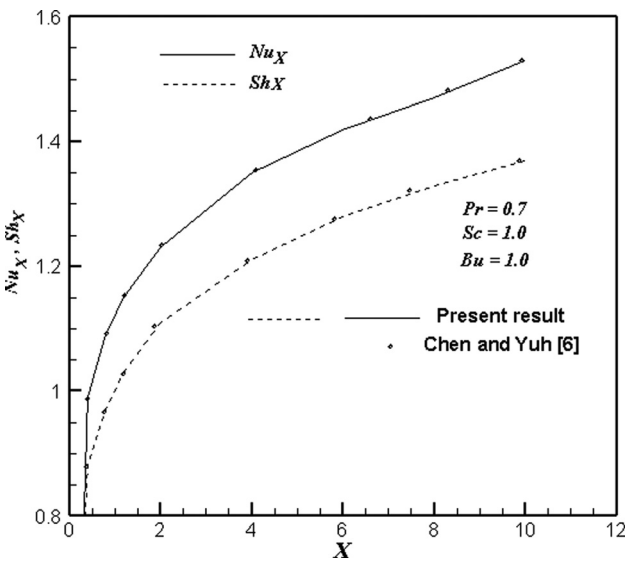

Fig. 8 Comparison of the local Nusselt (Nu_X) and Sherwood number (Sh_X)

Table 1 Comparison of average skin-friction coefficient ($\overline{C_f}$), Nusselt number ($\overline{\mathrm{Nu}}$), and Sherwood number ($\overline{\mathrm{Sh}}$)

	Sc	Pr	Bu	$\overline{C_f}$	$\overline{\mathrm{Nu}}$	$\overline{\mathrm{Sh}}$
Ganesan and Rani [33]	0.6	0.7	2.0	1.9321	1.0211	0.9047
Present	0.6	0.7	2.0	1.9321	1.0211	0.9047

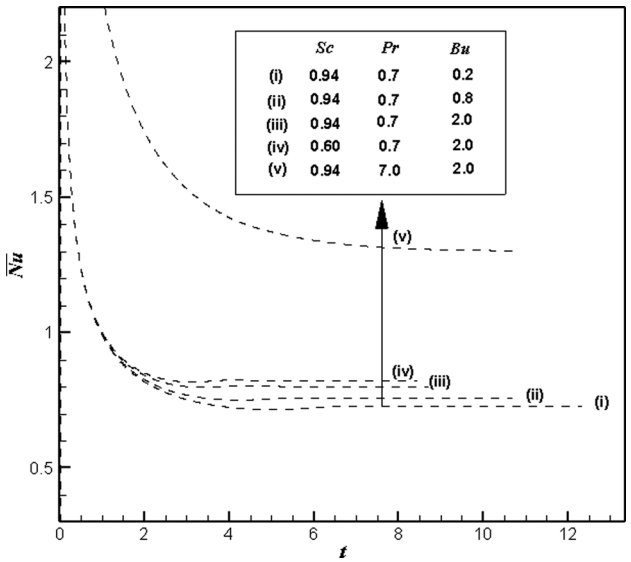

Fig. 9 The simulated average Nusselt number ($\overline{Nu}$)

In Fig. 9, the effects of Sc, Pr, and Bu on the simulated average heat transfer rate are shown. Here, the average Nusselt number has the same trend as the average skin-friction with respect to Sc but it increases as Pr increases. It is observed that for short period of time after $t=0$ the average Nusselt numbers are almost the same in cases with an identical Pr. This shows that initially heat conduction dominates in comparison with convection. An increase in Pr speeds up the spatial decay of the temperature near the heated surface together with the increased flow velocity near the wall, yielding an increase in the rate of heat transfer. In Fig. 10, the effects of Sc, Pr, and Bu on the average mass transfer rate are presented. Here, during an initial period of time mass diffusion is dominating in comparison to mass convection. For fixed Sc, the average Sherwood numbers are similar for short period of the time after $t=0$. It is noticed that for increasing values of Sc the average mass transfer rate increases, which is in line with the increase in the concentration gradient near the wall shown in Fig. 6(*b*). Also, the average mass transfer rate increases with increasing values of Bu, accompanied with an increased axial velocity.

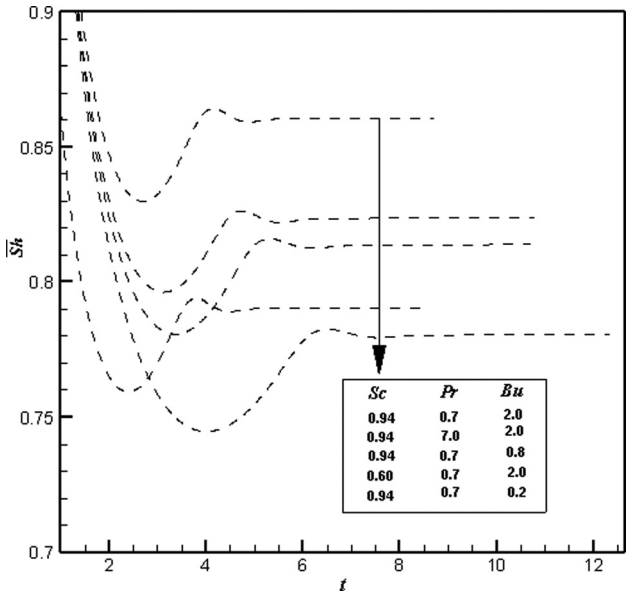

Fig. 10 The simulated average Sherwood number ($\overline{Sh}$)

4.3 Stream, Heat, and Mass Functions at the Final Steady-State. The fluid motion can be displayed using the nondimensional stream function ψ^*, which satisfies the continuity Eq. (10). The relationships between the stream function, ψ^*, and velocity components for two-dimensional flows are

$$U=\frac{1}{R}\frac{\partial\psi^*}{\partial R}\quad\text{and}\quad V=-\frac{1}{R}\frac{\partial\psi^*}{\partial X} \tag{15}$$

which yield a single equation

$$\frac{\partial^2\psi^*}{\partial X^2}+\frac{\partial^2\psi^*}{\partial R^2}=U+R\frac{\partial U}{\partial R}-R\frac{\partial V}{\partial X} \tag{16}$$

The heat function H' is defined through its first-order derivatives as

$$\frac{\partial H'}{\partial x}=\rho r v c_p\left(T'-T'_\infty\right)-k_f r\frac{\partial T'}{\partial r} \tag{17a}$$

$$-\frac{1}{r}\frac{\partial H'}{\partial r}=\rho u c_p\left(T'-T'_\infty\right) \tag{17b}$$

The heat function H' satisfies the steady energy balance equation (Eq. (3)). Introducing the nondimensional heat function $H^*=\left(H'/(k_f\left(T'_w-T'_\infty\right)r_0\mathrm{Gr_T})\right)$, in an attempt to make heat function as dimensionless so that its maximum value equals to the overall Nusselt number on the hot wall (see Refs. [22] and [27]) transforms Eqs. (17*a*) and (17*b*) into the following equations:

$$\frac{\partial H^*}{\partial X}=\mathrm{Pr}(RVT)-R\frac{\partial T}{\partial R} \tag{18a}$$

$$-\frac{\partial H^*}{\partial R}=\mathrm{Pr}(RUT) \tag{18b}$$

Note that the nondimensional heat function H^*, defined by Eqs. (18*a*) and (18*b*) identically satisfies the steady-state form of the nondimensional energy equation (Eq. (12)). From Eqs. (18*a*) and (18*b*), one obtains the following second-order partial differential equation of the heat function H^* for a medium of constant thermal conductivity:

$$\frac{\partial^2H^*}{\partial X^2}+\frac{\partial^2H^*}{\partial R^2}=\mathrm{Pr}\left[R\frac{\partial}{\partial X}(VT)-R\frac{\partial}{\partial R}(UT)-UT\right]-R\frac{\partial^2T}{\partial X\partial R} \tag{19}$$

Similarly, the concept of heat function can be extended to mass function M' which can be defined through its first-order derivatives as

$$\frac{\partial M'}{\partial x}=rv\left(C'-C'_\infty\right)-rD\frac{\partial C'}{\partial r} \tag{20a}$$

$$-\frac{1}{r}\frac{\partial M'}{\partial r}=u\left(C'-C'_\infty\right) \tag{20b}$$

To make mass function as dimensionless, the nondimensional number $M^*=\left(M'/(D\left(C'_w-C'_\infty\right)r_0\mathrm{Gr_T})\right)$ is introduced in such a way that its maximum value equals the overall Sherwood number on the hot wall. Then Eqs. (20*a*) and (20*b*) can be rewritten as

$$\frac{\partial M^*}{\partial X}=\mathrm{Sc}(RVC)-R\frac{\partial C}{\partial R} \tag{21a}$$

$$-\frac{\partial M^*}{\partial R}=\mathrm{Sc}(RUC) \tag{21b}$$

The nondimensional mass function M^* satisfies the steady-state form of the nondimensional concentration equation (Eq. (13)). From Eqs. (21*a*) and (21*b*), we can get the following second-order

partial differential equation of the mass function M^* for a medium of constant diffusion coefficient:

$$\frac{\partial^2 M^*}{\partial X^2} + \frac{\partial^2 M^*}{\partial R^2} = \mathrm{Sc}\left[R\frac{\partial}{\partial X}(VC) - R\frac{\partial}{\partial R}(UC) - UC\right] - R\frac{\partial^2 C}{\partial X \partial R} \tag{22}$$

To obtain the values of ψ^*, H^*, and M^*, the derivatives involved in Eqs. (16), (19), and (22) are evaluated using the second-order central differences. The boundary conditions of H^* and M^* are taken from the Eqs. (18) and (21). Further details can be found elsewhere [22,27]. Most of the results reported here are presented in terms of the plots of streamlines, heatlines, and masslines. These two heat and mass functions were found to provide a better visual representation of the heat and mass transfer phenomena compared to the isotherm and concentration contour plots.

Figure 11 illustrates the final steady-state streamlines (ψ^*) and heatlines (H^*) for different values of Sc, Pr, and Bu. From all these Figs. 11(*a*)–11(*d*), it is observed that the variation of heat function in a region occur very close to the hot wall is higher in comparison to that of streamlines, since the velocity near the wall is lower because of no-slip condition at the wall, while near the surface the heat flux is not very small. The streamlines are more dense in the region of $2 < R < 4$ that includes the peak velocity. However, the hot wall presence is weakly felt at the exterior edge of the velocity boundary layer. The rate of heat transfer from the hot wall to the fluid is highest at the leading edge and is decreased with an increase in the axial position. Therefore, the heatlines near the wall are dense for lower X value. From Figs. 11(*a*) and 11(*b*), it is observed that as Sc increases, the maximum value of the heat function H^* decreases, since the average Nusselt number, $\overline{\mathrm{Nu}}$, decreases on the hot wall ($R = 1$) which is shown in Table 2. Figures 11(*b*) and 11(*c*) shows that as Pr increases, the maximum value of the heat function H^* increases since $\overline{\mathrm{Nu}}$ increases with Pr. Also it is observed that the deviation of heatlines from the hot wall is more for higher values of Pr. Similarly, from Figs. 11(*b*) and 11(*d*), it is observed that as Bu increases the maximum value of the heat function H^* increases since $\overline{\mathrm{Nu}}$ increases with Bu.

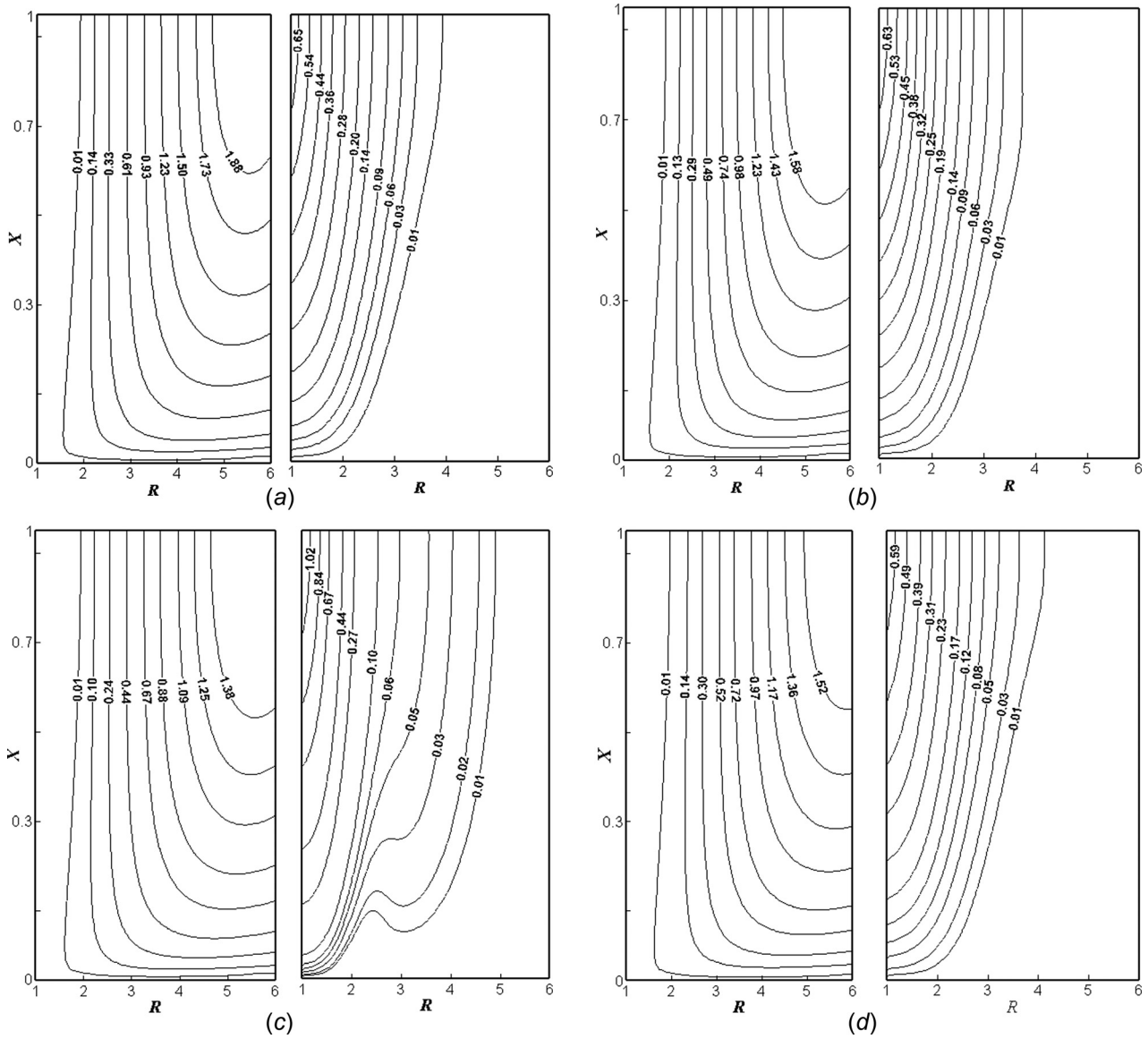

Fig. 11 Steady-state streamlines (ψ^*) (left) and heatlines (H^*) (right) for (*a*) Sc = 0.6, Pr = 0.7, Bu = 2.0; (*b*) Sc = 0.94, Pr = 0.7, Bu = 2.0; (*c*) Sc = 0.94, Pr = 7.0, Bu = 2.0; and (*d*) Sc = 0.94, Pr = 0.7, Bu = 0.8

Table 2 Simulated average skin-friction coefficient ($\overline{C_f}$), Nusselt number ($\overline{Nu}$), and Sherwood number ($\overline{Sh}$) in steady-state with different Sc, Pr, and Bu values for (a) couple stress fluid and (b) Newtonian fluid

Sc	Pr	Bu	$\overline{C_f}$	$\overline{Nu}$	$\overline{Sh}$
(a) Couple stress fluid					
0.6	0.7	2.0	0.4240	0.8213	0.7904
0.94	0.7	2.0	0.3932	0.8008	0.8607
0.94	7.0	2.0	0.3322	1.3036	0.8239
0.94	0.7	0.8	0.2844	0.7581	0.8139
0.94	0.7	0.2	0.2212	0.7280	0.7807
(b) Newtonian fluid					
0.6	0.7	2.0	1.9321	1.0211	0.9047
0.94	0.7	2.0	1.6142	0.8677	1.0597
0.94	7.0	2.0	1.4321	2.0677	0.9881
0.94	0.7	0.8	0.9821	0.7851	0.9671
0.94	0.7	0.2	0.7621	0.7533	0.9032

Figure 12 illustrates the final steady-state masslines M^* for different values of Sc, Pr, and Bu. From all these Figs. 12(*a*)–12(*d*), it is observed that the masslines have the same trend as that of heatlines. The masslines are showing mass extraction from the cylinder hot wall. Once again, and in similar lines with the heatlines for heat transfer visualization, the masslines indicate well bordered corridors where the mass is transported, and are the effective tools for mass transfer visualization and analysis, instead of the isoconcentration lines. Figures 12(*a*) and 12(*b*) shows that as Sc increases, the maximum value of the mass function M^* increases since the average Sherwood number $\overline{Sh}$ increases on the hotwall which is shown in Table 2. Also, it is observed that in Fig. 12(*b*), the masslines tend to move away from the hot wall for higher values of Sc which means that the mass transfer across the boundary layer is active. From Figs. 12(*b*) and 12(*c*), as Pr increases, the maximum value of the mass function M^* decreases since $\overline{Sh}$ decreases with Pr. Also, from Figs. 12(*b*) and 12(*d*), it is noticed that as Bu increases the maximum value of the mass function M^* increases since $\overline{Sh}$ increases with Bu.

Figures 11 and 12 illustrate that the heatlines and masslines can give a clear and complete picture of the heat and mass transfer processes occurring in the natural convection boundary layers adjacent to the hot wall.

4.4 Flow Comparison Between the Couple Stress and Newtonian Fluids. Figure 13 illustrates the final steady-state velocity, temperature, and concentration contours for the couple stress and Newtonian fluid flows with fixed Sc = 0.6, Pr = 0.7, and Bu = 2.0. It can be noticed that from Figs. 13(*a*) and 13(*b*), the velocity of the couple stress fluid is much smaller compared to that of the Newtonian fluid. This is due to the fact that in couple stress fluid flow there is additive diffusion terms (biharmonic term) compared with the Newtonian fluid (refer Eq. (11)). Also, from Figs. 13(*a*) and 13(*b*), it is observed that steady-state temperature and concentration contours for the couple stress fluid are somewhat different, with thicker temperature and concentration layers, from those for the Newtonian fluid.

Table 2 demonstrates the comparison between the couple stress fluid and Newtonian fluid in terms of average skin-friction coefficient, average heat, and mass transfer rates with different values of Sc, Pr, and Bu, where these values are tabulated in Table 2 for couple stress fluid and Newtonian fluid. From these Table 2, it is observed that the average values of skin-friction coefficient, Nusselt number, and Sherwood number of a couple stress fluid are smaller than those of the Newtonian fluid for all values of Sc, Pr, and Bu. In summary, Table 2 reveals that the characteristics of skin-friction, heat and mass transfer of a couple stress fluid differ from those of the Newtonian fluids.

Table 3 explains the variation of couple stress fluid flow from Newtonian fluid flow in terms of the time for the flow variables U, T, and C to reach the temporal maximum and the steady-state with different Sc, Pr, and Bu values, in which Table 3 tabulates the values for couple stress fluid and Newtonian fluid, respectively. Table 3 shows that the time required for all the flow variables to reach the temporal maxima and steady-state increases with increasing values of Sc and Pr. However, the reverse trend is observed for Bu. Also, from Table 3, we can see that with all values of Sc, Pr, and Bu the times for all the flow variables to reach the temporal maxima for the couple stress fluid are larger than those for the Newtonian fluid. It is also noticed that the times required for all the flow variables to reach the steady-state for the couple stress fluid are rather smaller than those for the Newtonian fluid, which means that the transient periods after the temporal maxima are quite longer for the Newtonian fluid compared to those for the couple stress fluid. Also, for all values of Sc, Pr, and Bu, the maximum velocities occur at

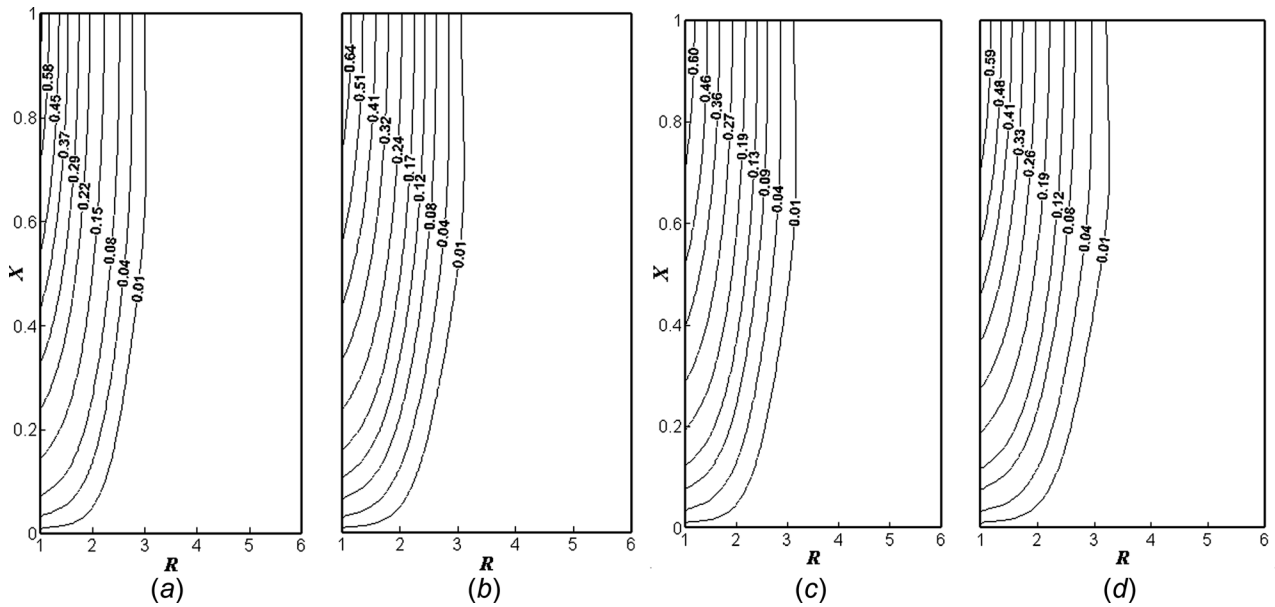

Fig. 12 Steady-state masslines (M^*) for (*a*) Sc = 0.6, Pr = 0.7, Bu = 2.0; (*b*) Sc = 0.94, Pr = 0.7, Bu = 2.0; (*c*) Sc = 0.94, Pr = 7.0, Bu = 2.0; and (*d*) Sc = 0.94, Pr = 0.7, Bu = 0.8

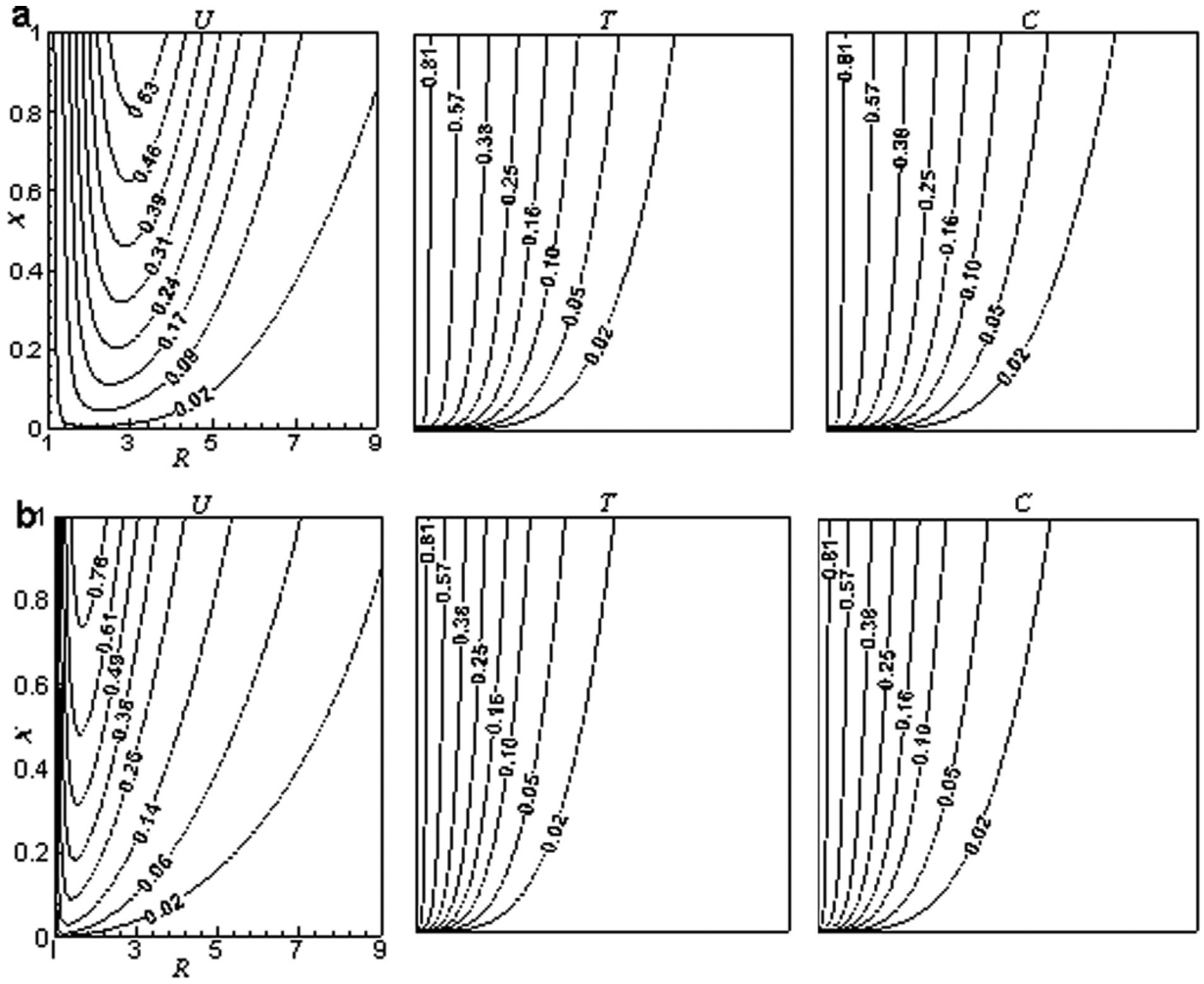

Fig. 13 Steady-state velocity (*U*), temperature (*T*), and concentration (*C*) contours with Sc = 0.6, Pr = 0.7, and Bu = 2.0 for (*a*) couple stress fluid and (*b*) Newtonian fluid

Table 3 The time needed for the flow variables to reach the temporal maxima and the steady-state; the maximum velocity with different Sc, Pr, and Bu values for (a) couple stress fluid and (b) Newtonian fluid

			Temporal maximum (t) of				
Sc	Pr	Bu	U	T	C	Steady-state time (t)	Maximum velocity (U) at $X = 1.0$
(a) Couple stress fluid							
0.60	0.7	2.0	3.47	3.52	3.22	8.44	0.5988
0.94	0.7	2.0	3.74	3.76	3.54	8.71	0.5377
0.94	7.0	2.0	4.28	4.32	4.07	10.80	0.4472
0.94	0.7	0.8	4.84	4.86	4.51	10.70	0.4381
0.94	0.7	0.2	6.03	6.04	5.50	12.35	0.3751
(b) Newtonian fluid							
0.60	0.7	2.0	2.22	2.04	1.88	10.94	0.8814
0.94	0.7	2.0	2.30	2.11	1.93	12.33	0.8355
0.94	7.0	2.0	2.58	2.40	2.20	10.99	0.6407
0.94	0.7	0.8	2.97	2.75	2.53	13.71	0.7067
0.94	0.7	0.2	3.69	3.42	3.15	14.86	0.6332

$X = 1.0$ for a couple stress fluid are smaller compared with those of Newtonian fluid.

5 Conclusions

Extensive buoyancy-induced fluid flow with heat and mass flow visualization is employed to study the transient natural convection boundary layer flow of a couple stress, viscous, incompressible fluid over a semi-infinite vertical cylinder. A Crank–Nicolson type of implicit method is used to solve the system of coupled governing equations together with the tridiagonal and pentadiagonal algorithms. A heat and mass flow visualization based on the concept of heatlines and masslines at the final steady-state, which is extremely useful in understanding the phenomenon, is studied and is recommended for the natural convection as well as mixed and forced convection situations. The basic

characteristics of heat function and mass function are useful for perceiving the visualization results, and also it has been shown that the level of heatlines and masslines is a direct measure of the heat and mass transfer.

When properly made dimensionless, the numerical values of the heat and mass functions are related to the local or overall Nusselt and Sherwood numbers, which characterize the overall heat and mass transfer process. The flow visualization includes the plots of streamlines, heatlines, and masslines. The computations are carried out for the values of Sc (= 0.6 and 0.94), Pr (= 0.7 and 7.0), and Bu (= 0.2, 0.8, and 2.0).

From the present study, it is observed that for the velocity, temperature, and concentration profiles the time elapsed to reach the temporal maximum and the steady-state increases with increasing values of Sc and Pr. However, the opposite trend is observed for Bu. It is noticed that as Pr increases, velocity, and temperature profiles decrease and concentration increases. As Sc increases, the velocity and concentration are found to decrease while the temperature increases. Also, average values of the skin-friction and Nusselt number decrease while the Sherwood number increases with an increase in Sc values. It is observed that as Pr increases the average skin-friction coefficient and average mass transfer rate are decreasing while the average heat transfer rate is increasing. It is also found that the average skin-friction, average heat and mass transfer rates increase as Bu increases. Also, it is observed that as Pr and Sc increases the heatlines and masslines are extended to a region far from the hot wall, respectively. Particularly, this study reveals that the deviations of velocity, temperature, and concentration profiles of the couple stress fluid flow turn out to be considerable from those of the Newtonian fluid flow.

Acknowledgment

The authors are thankful to the reviewers for their valuable suggestions and comments to improve the quality of the manuscript.

Nomenclature

Bu = combined buoyancy ratio parameter
C = dimensionless species concentration
C' = species concentration
c_p = specific heat at constant pressure
$\underline{C_f}$ = dimensionless local skin-friction coefficient
$\overline{C_f}$ = dimensionless average skin-friction coefficient
D = binary diffusion coefficient
d_{ij} = rate of deformation tensor
g = acceleration due to gravity
$\mathrm{Gr_C}$ = mass Grashof number
$\mathrm{Gr_T}$ = thermal Grashof number
H' = heat function
H^* = dimensionless heat function
k_f = thermal conductivity of the fluid
m = trace of couple stress tensor
M' = mass function
M^* = dimensionless mass function
$\underline{m_{ij}}$ = couple stress tensor
$\overline{\mathrm{Nu}}$ = average Nusselt number
Nu_X = local Nusselt number
p = fluid pressure
Pr = Prandtl number
r = radial coordinate
R = dimensionless radial coordinate
r_0 = radius of cylinder
$\underline{\mathrm{Sc}}$ = Schmidt number
$\overline{\mathrm{Sh}}$ = average Sherwood number
Sh_X = local Sherwood number
t = dimensionless time
T = dimensionless temperature
t' = time
T' = temperature
t_{ij} = force stress tensor
u, v = velocity components along x, r directions, respectively
U, V = dimensionless velocity components along X, R directions, respectively
$\mathbf{U}$ = velocity vector
x = axial coordinate
X = dimensionless axial coordinate

Greek Symbols

α = thermal diffusivity
β_C = volumetric coefficient of expansion with concentration
β_T = volumetric coefficient of thermal expansion
δ_{ij} = Kronecker delta
ε_{ijk} = Levi-Civita symbol
η, η' = couple stress viscosity coefficients
μ, λ = viscosity coefficients
ν = kinematic viscosity
ρ = density
ψ^* = dimensionless stream function
ω = spin vector
$\omega_{i,j}$ = spin tensor

Subscripts

w = conditions on the wall
∞ = free stream conditions

References

[1] Sparrow, E. M., and Gregg, J. L., 1956, "Laminar Free Convection Heat Transfer From the Outer Surface of a Vertical Circular Cylinder," ASME J. Heat Transfer, **78**(8), pp. 1823–1829.
[2] Minkowycz, W. J., and Sparrow, E. M., 1974, "Local Nonsimilar Solutions for Natural Convection on a Vertical Cylinder," ASME J. Heat Transfer, **96**(2), pp. 178–183.
[3] Fujii, T., and Uehara, H., 1970, "Laminar Natural Convective Heat Transfer From the Outer Surface of a Vertical Cylinder," Int. J. Heat Mass Transfer, **13**(3), pp. 607–615.
[4] Lee, H. R., Chen, T. S., and Armaly, B. F., 1988, "Natural Convection Along Slender Vertical Cylinders With Variable Surface Temperature," ASME J. Heat Transfer, **110**(1), pp. 103–108.
[5] Bottemanne, F. A., 1972, "Experimental Results of Pure and Simultaneous Heat and Mass Transfer by Free Convection About a Vertical Cylinder for Pr = 0.71 and Sc = 0.63," Appl. Sci. Res., **25**(1), pp. 372–382.
[6] Chen, T. S., and Yuh, C. F., 1980, "Combined Heat and Mass Transfer in Natural Convection Along a Vertical Cylinder," Int. J. Heat Mass Transfer, **23**(4), pp. 451–461.
[7] Gebhart, B., and Pera, L., 1971, "The Nature of Vertical Natural Convection Flows Resulting From the Combined Buoyancy Effects of Thermal and Mass Diffusion," Int. J. Heat Mass Transfer, **14**(12), pp. 2025–2050.
[8] Dring, R. P., and Gebhart, B., 1966, "Transient Natural Convection From Thin Vertical Cylinders," ASME J. Heat Transfer, **88**(2), pp. 246–247.
[9] Evan, L. B., Reid, R. C., and Drake, E. M., 1968, "Transient Natural Convection in a Vertical Cylinder," AIChE J., **14**(2), pp. 251–261.
[10] Rani, H. P., and Kim, C. N., 2009, "A Numerical Study of the Dufour and Soret Effects on Unsteady Natural Convection Flow Past an Isothermal Vertical Cylinder," Korean J. Chem. Eng., **26**(4), pp. 946–954.
[11] Eringen, A. C., 1966, "Theory of Micropolar Fluids," J. Math. Mech., **16**(1), pp. 1–18.
[12] Stokes, V. K., 1966, "Couple Stress in Fluids," Phys. Fluids, **9**(9), pp. 1709–1715.
[13] Chu, H. M., Li, W. L., and Hu, S. Y., 2006, "Effects of Couple Stresses on Pure Squeeze EHL Motion of Circular Contacts," J. Mech. **22**(1), pp. 77–84.
[14] Lin, J., 1998, "Squeeze Film Characteristics of Finite Journal Bearings: Couple Stress Fluid Model," Tribol. Int., **31**(4), pp. 201–207.
[15] Naduvinamani, N. B., and Patil, S. B., 2009, "Numerical Solution of Finite Modified Reynolds Equation for Couple Stress Squeeze Film Lubrication of Porous Journal Bearings," Comput. Struct., **87**(21), pp. 1287–1295.
[16] Chang-Jian, C., Yau, H., and Chen, J., 2010, "Nonlinear Dynamic Analysis of a Hybrid Squeeze-Film Damper-Mounted Rigid Rotor Lubricated With Couple Stress Fluid and Active Control," Appl. Math. Modell., **34**(9), pp. 2493–2507.
[17] Srivastava, V. P., 2003, "Flow of a Couple Stress Fluid Representing Blood Through Stenotic Vessels With a Peripheral Layer," Indian J. Pure Appl. Math., **34**(12), pp. 1727–1740.
[18] Srivastava, L. M., 1986, "Peristaltic Transport of a Couple Stress Fluid," Rheol. Acta, **25**(6), pp. 638–641.

[19] Umavathi, J. C., and Malashetty, M. S., 1999, "Oberbeck Convection Flow of a Couple Stress Fluid Through a Vertical Porous Stratum," Int. J. Non-Linear Mech., **34**(6), pp. 1037–1045.
[20] Habtu, A., and Radhakrishnamacharya, G., 2010, "Dispersion of a Solute in Peristaltic Motion of a Couple Stress Fluid Through a Porous Medium With Slip Condition," Int. J. Chem. Biol. Eng., **3**(4), pp. 205–210.
[21] Tasawar, H., Muhammad, A., Ambreen, S., and Hendi, Awatif A., 2012, "Unsteady Three Dimensional Flow of Couple Stress Fluid Over a Stretching Surface With Chemical Reaction," Nonlinear Anal., **17**(1), pp. 47–59.
[22] Kimura, S., and Bejan, A., 1983, "The Heatline Visualization of Convective Heat Transfer," ASME J. Heat Transfer, **105**(4), pp. 916–919.
[23] Bejan, A., 1984, *Convection Heat Transfer*, 1st ed., Wiley, New York, pp. 22, 23, 450, and 452.
[24] Trevisan, O. V., and Bejan, A., 1987, "Combined Heat and Mass Transfer by Natural Convection in a Vertical Enclosure," ASME J. Heat Transfer, **109**(1), pp. 104–112.
[25] Costa, V. A. F., 2000, "Heatline and Massline Visualization of Laminar Natural Convection Boundary Layers Near a Vertical Wall," Int. J. Heat Mass Transfer, **43**(20), pp. 3765–3774.
[26] Costa, V. A. F., 2006, "Bejan's Heatlines and Masslines for Convection Visualization and Analysis," ASME Appl. Mech. Rev., **59**(3), pp. 126–145.
[27] Aggarwal, S. K., and Manhapra, A., 1989, "Use of Heatlines for Unsteady Buoyancy-Driven Flow in a Cylindrical Enclosure," ASME J. Heat Transfer, **111**(2), pp. 576–578.
[28] Aggarwal, S. K., and Manhapra, A., 1989, "Transient Natural Convection in a Cylindrical Enclosure Nonuniformly Heated at the Top Wall," Numer. Heat Transfer, Part A, **15**(3), pp. 341–356.
[29] Mukhopadhyay, A., Qin, X., Aggarwal, S. K., and Puri, I. K., 2002, "On Extension of Heatline and Massline Concepts to Reacting Flows Through Use of Conserved Scalars," ASME J. Heat Transfer, **124**(4), pp. 791–799.
[30] Basak, T., Singh, A. K., Richard, R., and Roy, S., 2013, "Finite Element Simulation With Heatlines and Entropy Generation Minimization During Natural Convection Within Porous Tilted Square Cavities," Ind. Eng. Chem. Res., **52**(23), pp. 8046–8061.
[31] Singh, C., 1982, "Lubrication Theory for Couple Stress Fluids and Its Applications to Short Bearing," Wear, **88**(3), pp. 281–290.
[32] Stokes, V. K., 1984, *Theories of Fluids With Microstructure*, Springer-Verlag, New York.
[33] Ganesan, P., and Rani, H. P., 1998, "Transient Natural Convection Along Vertical Cylinder With Heat and Mass Transfer," Heat Mass Transfer, **33**(5–6), pp. 449–455.